

Three-Dimensional SAR Imaging with Sparse Linear Array using Tensor Completion in Embedded Space

Siqian Zhang (✉ zhangsiqian@nudt.edu.cn)

National University of Defense Technology <https://orcid.org/0000-0001-8108-9278>

Ding Ding

National University of Defense Technology

Chenxi Zhao

National University of Defense Technology

Lingjun Zhao

National University of Defense Technology

Research Article

Keywords: 3-D imaging, sparse data, low rank, tensor completion, synthetic aperture radar (SAR).

Posted Date: March 29th, 2022

DOI: <https://doi.org/10.21203/rs.3.rs-1449510/v1>

License: © ⓘ This work is licensed under a Creative Commons Attribution 4.0 International License.

[Read Full License](#)

Three-Dimensional SAR Imaging with Sparse Linear Array using Tensor Completion in Embedded Space

Siqian Zhang^{1*}, Ding Ding², Chenxi Zhao¹ and Lingjun Zhao¹

Abstract

Due to the huge data storage and transmission pressure, sparse data collection strategy has provided opportunities and challenges for 3-D SAR imaging. However, sparse data brought by the sparse linear array will produce high-level side-lobes, as well as the aliasing and the false-alarm targets. Simultaneously, the vectorizing or matrixing of 3-D data makes high computational complexity and huge memory usage, which is not practicable in real applications. To deal with these problems, tensor completion (TC), as a convex optimization problem, is used to solve the 3-D sparse imaging problem efficiently. Unfortunately, the traditional TC methods are invalid to the incomplete tensor data with missing slices brought by sparse linear arrays. In this paper, a novel 3-D imaging algorithm using TC in embedded space is proposed to produce 3-D images with efficient side-lobes suppression. With the help of sparsity and low-rank property hidden in the 3-D radar signal, the incomplete tensor data is taken as the input and converted into a higher order incomplete Hankel tensor by multiway delay embedding transform (MDT). Then, the Tucker decomposition with incremental rank has been applied for completion. Subsequently, any traditional 3-D imaging methods can be employed to obtain excellent imaging performance for the completed tensor. The proposed method achieves high resolution and low-level side-lobes compared with the traditional TC-based methods. It is verified by several numerical simulations and multiple comparative studies on real data. Results clearly demonstrate that the proposed method can generate 3-D images with small reconstruction error even when the sparse sampling rate or signal to noise ratio is low, which confirms the validity and advantage of the proposed method.

Keywords: 3-D imaging, sparse data, low rank, tensor completion, synthetic aperture radar (SAR).

1 Introduction

Three-dimensional synthetic aperture radar (3-D SAR) imaging can provide a high resolution 3-D imagery of an interest target or scene, which has an important significance for military and civilian practical applications. In recent years, many 3-D SAR imaging techniques have emerged, such as interferometric SAR (InSAR) [1, 2], Tomographic SAR [3], Circular SAR (CSAR) [4-6] and Linear Array SAR (LASAR) [7-9]. The first two SAR systems based on the interferometry technology use multiple antennas looking at the scene with slightly different view angles to estimate the 3-D altimetric profile of the imaged scene [1]. However, the

*Correspondence: zhangsiqian@nudt.edu.cn

¹ State Key Laboratory of Complex Electromagnetic Environment Effects on Electronics and Information System, College of Electronic Science, National University of Defense Technology, Changsha 410073, China.
Full list of author information is available at the end of the article.

generation of the digital elevation model depends on precise baseline estimation and the scatterer distribution along the height direction cannot be obtained [1-3]. CSAR, employing the circular aperture via the maneuver trajectory on the azimuth-height plane, has a large aperture both in the azimuth and height direction to obtain a 3-D imaging capability [10]. It is difficult to control the precise flight trajectory. To overcome these restrictions, downward-looking linear array (DLLA) 3-D SAR is presented by Gierull [11]. DLLA 3-D SAR [12-14] combines the concepts of real and synthetic aperture to generate a virtual 2-D aperture and can provide high-resolution radar images in three dimensions. In addition, the shadowing effects caused by the side-looking mode of the traditional SAR system can be alleviated by looking downward.

Moreover, the drawbacks of huge data storage and transmission burden make the LASAR system meet many difficulties in the practical application as it demands a dense sampling data in three dimensions. As a result, sparse data collection strategy can reduce the burden of data collection significantly, which creates powerful incentives to research 3-D SAR imaging with the sparse linear array. Unfortunately, when the conventional imaging algorithms meet sparsely collected data, the performance of 3-D images is degraded drastically with unpredictable sidelobe and false targets behavior. Since the sampling rate no longer satisfies the Nyquist sampling rate, much worse, the targets even cannot be focused.

Many sparse reconstruction methods have merged as the times required. The methods for reconstructing sparse signal can be categorized into two classes. In the first class, the methods directly recover a sparse signal with an overwhelming probability by a limited number of measurements based on compressive sensing (CS) theory [15-17]. However, the quality of the 3-D image may be seriously affected by the accuracy of its measurement matrix. By contrast, the methods in the second class complete the missing samples of a sparse signal using only its available elements. The key is to build up the relationship between the available and the missing entries [18]. As a representative technique, matrix/tensor completion utilizes the low-rank priors to characterize the relationship between the available and the missing entries [19]. Meanwhile, tensor [18] can preserve the internal structure of the multidimensional data without vectorization or matricization. Therefore, for sparse signal, if the low-rank property of an echoed data tensor is satisfied, the missing elements can be recovered from the known samples by solving a convex optimization problem [20]. Some heuristic algorithms [18, 21-24] such as the nuclear-norm and total variation regularization methods were proposed to estimate the missing values iteratively and have been proven to be effective in 3-D SAR sparse imaging applications [12, 25, 26]. However, in fact the echoed data acquired by the sparse linear array can be regarded as a 3-order incomplete tensor with randomly missing slices. In this case, the tensor completion methods mentioned above usually fail to recover the missing data element, which cause the unacceptable imaging performance. Fortunately, a good thought for data completion has been proposed by applying multi-dimensional Hankelization on an incomplete data [27, 28].

In this paper, a novel imaging algorithm using TC in embedded space is proposed for DLLA 3-D SAR with a sparse linear array. Firstly, the signal model of the 3-D sparse echo data is modeled and converted from the Euclidean space to the tensor space. With the help of tensor, the internal properties hidden in the 3-D data can be investigated. Secondly, the incomplete data with missing slices is represented as a higher order Hankel tensor via multiway delay embedding transform (MDT). Due to the Hankel structure, it is expected that the resulting higher order tensor has relatively low rank. Then the missing elements are completed perfectly by a Tucker decomposition in the embedded space. In the following, the 3-D image can be obtained by the traditional Fourier transform-based algorithms. Finally, the validity and the advantage of the proposed algorithm have been verified by the 3-D scene simulated and real data.

The paper is organized as follows. Section 2 introduces the notations and related backgrounds of the tensor that will be used in this paper. In section 3, the 3-D signal model of DLLA 3-D SAR with a sparse linear array is established in the tensor space. In section 4, we discuss the low rank and sparse property and then present a 3-D imaging algorithm using TC in embedded space for DLLA 3-D SAR with a sparse linear array. Section 5 shows the simulation and experiments to confirm the validity of the proposed

method. Finally, conclusions are made in Section 6.

2 Notation and Preliminaries

A vector is denoted by a boldface lowercase letter \mathbf{a} . A matrix is denoted by a boldface capital letter \mathbf{A} . A tensor is denoted by a boldface Euler script letter \mathcal{X} . The order of a tensor is the number of dimensions. The i th entry of a vector \mathbf{a} is denoted by a_i , the (i, j) th element of a matrix \mathbf{A} by a_{ij} , and the (i_1, i_2, \dots, i_N) th element of an N th-order tensor \mathcal{X} is denoted by $x_{i_1 i_2 \dots i_N}$. The n th element in a sequence is denoted by a superscript in parentheses, e.g., $\mathbf{A}^{(n)}$ denotes the n th matrix in a sequence $\{\mathbf{A}\} = \{\mathbf{A}_1, \mathbf{A}_2, \dots, \mathbf{A}_N\}$. *Slices* are two-dimensional sections of a tensor, defined by fixing all but two indices. The Frobenius norm of an N th-order tensor is the square root of the sum of the squares of all its elements, which is defined by

$$\|\mathcal{X}\|_F = \sqrt{\sum_{i_1=1}^{I_1} \sum_{i_2=1}^{I_2} \dots \sum_{i_N=1}^{I_N} x_{i_1 i_2 \dots i_N}^2}.$$

Matricization: The mode- k unfolding (*matricization*) of a tensor $\mathcal{X} \in \mathbb{C}^{I_1 \times I_2 \times \dots \times I_N}$ is denoted by $\mathbf{X}_{(n)}$ and arranges the mode- k fibers to be the columns of the matrix. Tensor elements (i_1, i_2, \dots, i_N) map to matrix elements (i_n, j) where

$$j = 1 + \sum_{k=1, k \neq n}^N (i_k - 1)J_k, \text{ with } J_k = \prod_{m=1, m \neq n}^{k-1} I_m.$$

Tensor multiplication: The n -mode product of a tensor $\mathcal{X} \in \mathbb{C}^{I_1 \times I_2 \times \dots \times I_N}$ with a matrix $\mathbf{A} \in \mathbb{C}^{J \times I_n}$ is denoted by $\mathcal{X} \times_n \mathbf{A}$ and is of size $I_1 \times \dots \times I_{n-1} \times J \times I_{n+1} \times \dots \times I_N$, where

$$(\mathcal{X} \times_n \mathbf{A})_{i_1 \dots i_{n-1} j_{n+1} \dots i_N} = \sum_{i_n=1}^{I_n} x_{i_1 i_2 \dots i_N} a_{j i_n} \quad (1)$$

Tucker decomposition: The tucker decomposition is denoted by

$$\mathcal{X} = \mathcal{G} \times_1 \mathbf{A}^{(1)} \times_2 \mathbf{A}^{(2)} \dots \times_N \mathbf{A}^{(N)} \quad (2)$$

where the tensor $\mathcal{G} \in \mathbb{C}^{R_1 \times R_2 \times \dots \times R_N}$ is called the *core tensor* and $\{\mathbf{A}^{(n)}\}_{n=1}^N$ is a set of the *factor matrices*.

The matricized version of (2) is

$$\mathbf{X}_{(n)} = \mathbf{A}^{(n)} \mathbf{G}_{(n)} \left(\mathbf{A}^{(1)} \otimes \dots \otimes \mathbf{A}^{(n-1)} \otimes \mathbf{A}^{(n+1)} \otimes \dots \otimes \mathbf{A}^{(N)} \right)^T \quad (3)$$

where \otimes denotes the Kronecker product.

Multi-linear tensor product: Consider $\{\mathbf{U}^{(n)}\}_{n=1}^N \in \mathbb{C}^{I_n \times R_n}$ and an N th-order tensor $\mathcal{G} \in \mathbb{C}^{R_1 \times R_2 \times \dots \times R_N}$, the multi-linear tensor product is defined as

$$\mathcal{G} \times \{\mathbf{U}\} = \mathcal{G} \times_1 \mathbf{U}^{(1)} \times_2 \mathbf{U}^{(2)} \dots \times_N \mathbf{U}^{(N)} \quad (4)$$

Moreover, a multi-linear tensor product excluding the n -th mode is defined as

$$\mathcal{G} \times_{-n} \{\mathbf{U}\} = \mathcal{G} \times_1 \mathbf{U}^{(1)} \dots \times_{n-1} \mathbf{U}^{(n-1)} \times_{n+1} \mathbf{U}^{(n+1)} \dots \times_N \mathbf{U}^{(N)} \quad (5)$$

where \mathcal{G} and $\mathbf{U}^{(n)}$ are referred to as the core tensor and factor matrices respectively when we consider Tucker decomposition.

Rank-one tensors: An N -way tensor $\mathcal{X} \in \mathbb{C}^{I_1 \times I_2 \times \dots \times I_N}$ is *rank one* if it can be written as the outer product of N vectors, i.e.,

$$\mathcal{X} = \mathbf{a}^{(1)} \circ \mathbf{a}^{(2)} \circ \dots \circ \mathbf{a}^{(N)} \quad (6)$$

The symbol \circ represents the vector outer product. This means that each element of the tensor is the product of the corresponding vector elements:

$$x_{i_1 i_2 \dots i_N} = a_{i_1}^{(1)} a_{i_2}^{(2)} \dots a_{i_N}^{(N)} \text{ for all } 1 \leq i_n \leq I_n \quad (7)$$

Tensor rank: The *rank* of a tensor \mathcal{X} , denoted $\text{rank}(\mathcal{X})$, is defined as the smallest number of rank-one tensor that generate \mathcal{X} as their sum.

3 Signal Model

The geometry of downward-looking sparse linear array 3-D SAR is shown in Fig.1. The plane is supposed to fly at the altitude H along the azimuth direction (X-axis) with the velocity v . The sparse array antenna is mounted underneath the wings along the cross-track direction (Y-axis). Z-axis denotes the height direction and the origin of the coordination O is the center of the imaging scene.

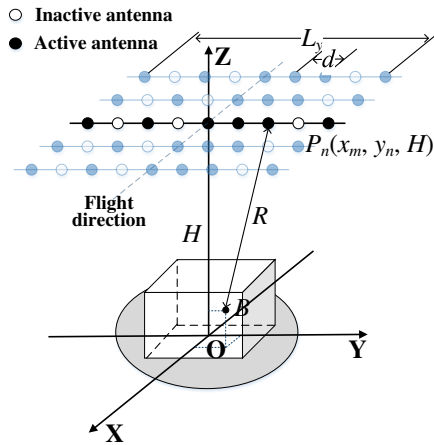


Fig.1 Geometric mode of downward-looking sparse linear array 3-D SAR

According to the scattering center model theory [29], a volumetric target can be numerically divided into finite scattering points for target profile reconstruction. Let the active antenna sends a step-frequency signal at location $P_n = (x_m, y_n, H)$ with $x_m = vt_m$, $y_n = -L_y d/2 + (n-1)d$, after a delay of round trip $2R/c$, the echo from a strong scattering point at $B(x, y, z)$ is expressed as

$$S_r = A\sigma \exp[-j2\pi(f_0 + k\Delta f)(t - 2R/c)] \quad (8)$$

where σ is the reflection coefficient of the scattering point. A sequence of modulated signals consists of a group of K pulses with the frequencies increased successively by a constant frequency increment Δf . f_0 is the basic frequency of the signals. R is the distance between the active antenna and the scattering point, as

$$\begin{aligned} R &= \sqrt{(x_m - x)^2 + (y_n - y)^2 + (H - z)^2} \\ &= \sqrt{R_0^2 - 2(x_m x + y_n y + Hz) + x^2 + y^2 + z^2} \end{aligned} \quad (9)$$

where $R_0 = \sqrt{x_m^2 + y_n^2 + H^2}$ denotes the distance between the active antenna P_n and the original point O.

Based on the Taylor series expansion of (9) and the far-field approximation $R_0 \gg x, y, z$, it yields

$$R \approx R_0 - \left(\frac{x_m x}{R_0} + \frac{y_n y}{R_0} + \frac{Hz}{R_0} \right) \quad (10)$$

Actually, the frequency of transmitted signal and the 2-D synthetic aperture are sampled discretely. The received phase history data from this scattering point is denoted as

$$S_r(x_m, y_n, f) = \sum_{m=1}^M \sum_{n=1}^N \sum_{k=1}^K \sigma(x, y, z) \exp(-j4\pi Rf/c) \quad (11)$$

Let

$$\begin{cases} \alpha_{x,m} = 2 \frac{f}{c} \frac{x_m}{R_0} \\ \alpha_{y,n} = 2 \frac{f}{c} \frac{y_n}{R_0} \\ \alpha_{z,k} = 2 \frac{f}{c} \frac{H}{R_0} \end{cases} \quad (12)$$

For simplicity, the constant term $\exp(-j4\pi R_0/\lambda)$ can be ignored in the following discussion. Thus, the received data can be rewritten as

$$S_r(\alpha_{x,m}, \alpha_{y,n}, \alpha_{z,k}) = \sum_{m=1}^M \sum_{n=1}^N \sum_{k=1}^K \sigma(x, y, z) e^{j2\pi(\alpha_{x,m}x + \alpha_{y,n}y + \alpha_{z,k}z)} \quad (13)$$

which is the 3-D radar signal model in the Euclidean Space. It is evident that the received data can be converted into the tensor space. The image grid can be equally spaced in three-order tensor way, with the size of $P \times Q \times L$. Therefore, the received data in (13) can be rewritten as

$$y(m, n, k) = \sum_{p=1}^P \sum_{q=1}^Q \sum_{l=1}^L \sigma(p, q, l) e^{j2\pi(\alpha_{x,m}x_p + \alpha_{y,n}y_q + \alpha_{z,k}z_l)} \quad (14)$$

Eq. (14) can be arranged in tensor form as

$$\mathcal{Y} = \mathcal{W} \times_1 \Psi_a \times_2 \Psi_c \times_3 \Psi_r \quad (15)$$

where $\mathcal{Y} \in \mathbb{C}^{M \times N \times K}$ is the echo data tensor, $\mathcal{W} \in \mathbb{C}^{P \times Q \times L}$ is the target reflectivity coefficient tensor, \times_n denotes the n -mode product of a tensor, and $\Psi_a \in \mathbb{C}^{M \times P}$, $\Psi_c \in \mathbb{C}^{N \times Q}$, $\Psi_r \in \mathbb{C}^{K \times L}$ represent the steering vector matrices in the azimuth, cross-track, and range direction, respectively.

$$\begin{aligned} \Psi_a(m, p) &= \exp(\alpha_{x,m} \cdot x_p) \\ \Psi_c(n, q) &= \exp(\alpha_{y,n} \cdot y_q) \\ \Psi_r(k, l) &= \exp(\alpha_{z,k} \cdot z_l) \end{aligned} \quad (16)$$

4 Methods

Instead of reconstructing the target immediately, an alternative way is to recover the missing data elements at first and then apply the conventional 3-D imaging algorithm to reconstruct the perfect 3-D image. However, the echo data acquired by the sparse linear array can be regarded as a 3-order incomplete tensor with randomly missing slices. In this case, the traditional tensor completion methods usually fail to recover the missing data element, which cause the unacceptable imaging performance.

In this section, we present a novel 3-D SAR imaging algorithm using tensor completion in embedded space to solve the above problem. The flowchart of the proposed 3-D SAR imaging method for the echo data tensor with missing slice acquired by sparse linear array is shown in Fig. 2. The proposed imaging algorithm includes two parts: tensor completion and 3-D imaging, where the part of tensor completion comprises three steps: ① MDT, ② low-rank tensor approximation, and ③ inverse MDT. Firstly, we discuss the low-rank property of signal tensor, which is a prerequisite for tensor completion. Secondly, the incomplete echoed data is represented as a higher order Hankel tensor via MDT and then the low-rank tensor completion problem is solved in the embedded space by Tucker decomposition. Finally, a completed tensor can be obtained by using the inverse MDT of the recovered higher

order tensor. Thus, we can employ any traditional 3-D imaging method to obtain the excellent imaging performance for the completed tensor.

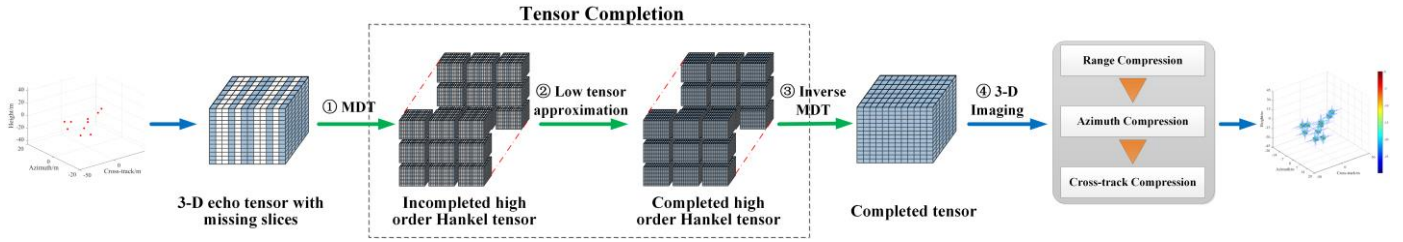


Fig.2 The flowchart of the proposed 3-D SAR imaging method.

4.1 Property Analysis for Signal Tensor

First, we discuss the sparse property based on the signal model in (14), which is helpful for 3-D image reconstruction from sparse signal tensors. For DLLA 3-D SAR imaging, there are large amounts of nontarget zones in the 3-D scene. That is to say, the 3-D radar image \mathcal{W} can be seen as the sum of back scattered responses of a few prominent scatters, where the signal contributions are expected as: 1) Strong returns from metallic structures or specular and dihedral or trihedral reflection can be regarded as points that would also be used in persistent scatterer interferometry. They are the dominating signal contributions. 2) Weak diffuse scattering from rough surfaces (roads and building roofs/walls) can be treated as discrete scatterers. 3) Returns from volumetric scatterers, e.g., from vegetation result in a continuous signal background in elevation. However, since these ensembles of scatterers often decorrelate in time, their response is treated as noise. The considerations mentioned above suggest that \mathcal{W} is expected to be sparse.

Then, the low-rank property is a prerequisite for tensor completion. For one scattering point, the signal data can be expressed as

$$y(m, n, k) = \sigma e^{j2\pi(\alpha_{x,m}x + \alpha_{y,n}y + \alpha_{z,k}z)} \quad (17)$$

It is clear that the signal tensor \mathcal{Y} can be expressed as an outer product of vectors.

$$\mathcal{Y} = \sigma \Psi_a(:, x) \circ \Psi_c(:, y) \circ \Psi_r(:, z) \quad (18)$$

where the symbol \circ represents the vector outer product. Since it is obvious that the tensor \mathcal{Y} is a rank-one three-mode tensor (see section 2), the tensor \mathcal{Y} is low rank.

Based on the multiple scattering points, the signal tensor can be regarded as a linear combination of rank-one three-mode tensors

$$\mathcal{Y} = \sum_{s=1}^S \sigma_{x_s y_s z_s} \Psi_a(:, x_s) \circ \Psi_c(:, y_s) \circ \Psi_r(:, z_s) \quad (19)$$

The rank of a tensor \mathcal{Y} is defined as the smallest number of rank-one tensors that generate \mathcal{Y} as their sum (see section 2). That is to say, the rank of tensor \mathcal{Y} is less than S . Whereas the imaging scene is composed of a few strong scattering points and thus $S \ll PQL$, indicating $rank(\mathcal{Y}) \leq S \ll PQL$. Therefore, the tensor \mathcal{Y} has a low CP-rank property as long as the targets are sparse.

Based on the above discussed property including the sparsity of \mathcal{W} and low-rank property of \mathcal{Y} , 3-D reconstruction from the sparse data tensor is feasible by solving optimization problems in the following subsections.

4.2 MDT and inverse MDT

Let us consider a tensor $\mathcal{Y} \in \mathbb{C}^{M \times N \times K}$, a delay embedding transform of tensor \mathcal{Y} with $\boldsymbol{\tau} = \{\tau_1, \tau_2, \tau_3\} \in \mathbb{N}^3$ can be decomposed into multi-linear duplication and multi-way folding operations [28], as shown in Fig.3.

First, the MDT produces a duplicated high order tensor from the low order tensor \mathcal{Y} , which is called as ‘‘Hankelization’’ [30]. Consider the duplication matrices are satisfied as

$$\begin{aligned} \mathbf{S}_1 &\in \{0,1\}^{\tau_1(M-\tau_1+1) \times M} \\ \mathbf{S}_2 &\in \{0,1\}^{\tau_2(N-\tau_2+1) \times N} \\ \mathbf{S}_3 &\in \{0,1\}^{\tau_3(K-\tau_3+1) \times K} \end{aligned} \quad (20)$$

Then the MDT can be obtained by

$$\mathcal{H}_{\boldsymbol{\tau}}(\mathcal{Y}) = \text{fold}_{(\boldsymbol{\Psi}, \boldsymbol{\tau})}(\mathcal{Y} \times_1 \mathbf{S}_1 \times_2 \mathbf{S}_2 \times_3 \mathbf{S}_3) \quad (21)$$

where $\text{fold}_{(\boldsymbol{\Psi}, \boldsymbol{\tau})}$ denotes a folding operator from a low order tensor to a high order one. Here a 6-th order tensor with $\tau_1 \times (M - \tau_1 + 1) \times \tau_2 \times (N - \tau_2 + 1) \times \tau_3 \times (K - \tau_3 + 1)$ is constructed from the input 3-th order tensor with $\tau_1(M - \tau_1 + 1) \times \tau_2(N - \tau_2 + 1) \times \tau_3(K - \tau_3 + 1)$.

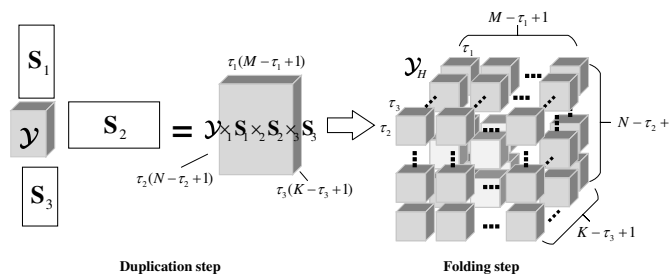


Fig.3 Multi-way delay embedding transform for a tensor.

In contrast, the inverse MDT transform can be decomposed into the individual corresponding inverse transforms: a matricization operation (also known as unfolding) and the Moore-Penrose pseudo-inverse $\mathbf{S}^\dagger = (\mathbf{S}^T \mathbf{S})^{-1} \mathbf{S}^T$. Thus, the inverse MDT for the Hankel tensor \mathcal{Y}_H is given by

$$\mathcal{H}_{\boldsymbol{\tau}}^{-1}(\mathcal{Y}_H) = \text{unfold}_{(\boldsymbol{\Psi}, \boldsymbol{\tau})}(\mathcal{Y}_H) \times_1 \mathbf{S}_1^\dagger \times_2 \mathbf{S}_2^\dagger \times_3 \mathbf{S}_3^\dagger \quad (22)$$

4.3 Low-rank Tensor Approximation

According to (21), the incomplete tensor $\mathcal{Y} \in \mathbb{C}^{M \times N \times K}$ and its mask tensor $\mathcal{Q} \in \{0,1\}^{M \times N \times K}$ can be transformed by MDT, which are given by

$$\begin{aligned} \mathcal{Y}_H &= \mathcal{H}(\mathcal{Y}) \in \mathbb{C}^{J_1 \times \dots \times J_I} \\ \mathcal{Q}_H &= \mathcal{H}(\mathcal{Q}) \in \{0,1\}^{J_1 \times \dots \times J_I} \end{aligned} \quad (23)$$

where $I \geq 3$. The zero elements in \mathcal{Q}_H correspond to the missing entry; otherwise, the one element correspond to the available entry.

A low-rank approximation of \mathcal{Y}_H based on Tucker decomposition model can be obtained by the following optimization problem:

$$\underset{\mathcal{G}, \{\mathbf{U}^{(i)}\}_{i=1}^L}{\text{minimize}} \left\| \mathcal{Q}_H \otimes (\mathcal{Y}_H - \mathcal{G} \times \{\mathbf{U}\}) \right\|_F^2, \text{ s.t. } \mathcal{G} \in \mathbb{R}^{R_1 \times \dots \times R_L}, \mathbf{U}^{(i)} \in \mathbb{R}^{J_i \times R_i} (\forall i) \quad (24)$$

where \otimes is the element wise Hadamard product.

The above optimization problem is not convex, its solution is not unique, and it is not easy to obtain its global solution [20]. For the tensor with the complete elements, the alternating least squares (ALS) [20] can efficiently obtain its stationary point for Tucker decomposition. Whereas for the tensor with missing elements, this optimization problem can be effectively solved by gradient descent method [31] and manifold optimization [32]. The efficiency of both algorithms is sensitive to the step-size parameter. Therefore, an auxiliary function [28] is introduced to perform Tucker decomposition with missing elements, which defined by

$$h(\theta|\theta') := \left\| \mathcal{Q}_H \otimes (\mathcal{Y}_H - \mathcal{X}_\theta) \right\|_F^2 + \left\| \bar{\mathcal{Q}}_H \otimes (\mathcal{X}_{\theta'} - \mathcal{X}_\theta) \right\|_F^2 \quad (25)$$

where $\theta = \{\mathcal{G}, \mathbf{U}^{(1)}, \dots, \mathbf{U}^{(L)}\}$ is a set of parameters, $\bar{\mathcal{Q}}_H = 1 - \mathcal{Q}_H$ represents a complement set of \mathcal{Q}_H , and $\mathcal{X}_\theta = \mathcal{G} \times \{\mathbf{U}\}$ is a Tucker decomposition.

According to [28], the auxiliary function can be transformed by

$$\begin{aligned} h(\theta|\theta') &= \left\| \mathcal{Q}_H \otimes (\mathcal{Y}_H - \mathcal{X}_\theta) \right\|_F^2 + \left\| \bar{\mathcal{Q}}_H \otimes (\mathcal{X}_{\theta'} - \mathcal{X}_\theta) \right\|_F^2 \\ &= \left\| (\mathcal{Q}_H \otimes \mathcal{Y}_H + \bar{\mathcal{Q}}_H \otimes \mathcal{X}_{\theta'}) - (\mathcal{Q}_H + \bar{\mathcal{Q}}_H) \otimes \mathcal{X}_\theta \right\|_F^2 \\ &= \left\| \mathcal{Z} - \mathcal{X}_\theta \right\|_F^2 \end{aligned} \quad (26)$$

Thus, the minimization of the auxiliary function can be regarded as two parts. First, the auxiliary tensor can be calculated by

$$\mathcal{Z} = \mathcal{Q}_H \otimes \mathcal{Y}_H + \bar{\mathcal{Q}}_H \otimes \mathcal{X}_{\theta'} \quad (27)$$

Then, the core tensor \mathcal{G} and the factor matrices $\{\mathbf{U}\}$ are updated by using the ALS to optimize

$$\underset{\mathcal{G}, \{\mathbf{U}^{(i)}\}_{i=1}^L}{\min} \left\| \mathcal{Z} - \mathcal{G} \times \{\mathbf{U}\} \right\|_F^2, \text{ s.t. } \mathbf{U}^{(i)T} \mathbf{U}^{(i)} = \mathbf{I}_{R_i} (\forall i) \quad (28)$$

In order to the non-uniqueness of the solution for the tensor \mathcal{X} , the rank increment strategy is integrated into Tucker-based completion, which has been discussed in [28]. The core feature is that the tensor should be initialized by a lower rank approximation than its target rank. Using the rank increment method, a Tucker decomposition with a very low-rank setting (e.g., rank-one tensor) is firstly obtained and a higher-rank decomposition is then obtained by using the previous lower-rank decomposition for its initialization. Following that a higher-rank decomposition is repeatedly obtained until the residual was sufficiently small. Therefore, the low-rank tensor completion with rank increment can be summarized as

Step 1: Set initial $R_i=1$ for all i .

Step 2: Obtain \mathcal{G} and $\{\mathbf{U}^{(i)}\}_{i=1}^L$ with (R_1, \dots, R_L) using eq. (27) and (28) and obtain $\mathcal{X} = \mathcal{G} \times \{\mathbf{U}\}$.

Step 3: Check the noise condition $\left\| \mathcal{Q}_H \otimes (\mathcal{Y}_H - \mathcal{X}) \right\|_F^2 \leq \varepsilon$, where ε is a noise threshold parameter. If it is satisfied, the algorithm is terminated; otherwise, go to the next step.

Step 4: Choose the incremental mode $i^{new} = \underset{i}{\operatorname{argmax}} \left\| (\mathcal{Q}_H \otimes (\mathcal{Y}_H - \mathcal{X})) \times_{-i} \{\mathbf{U}^T\} \right\|_F^2$ and increment $R_{i^{new}}$, and then go back to

step 2.

4.4 3-D Image Reconstruction

After the full-sampled 3-D data have been recovered by tensor completion mentioned above, 3-D image of target can be reconstructed by the compression technologies based on Fourier transform along the range, azimuth and cross-track direction, respectively. Additionally, the spectrum estimation strategies [33] also can be applied to achieve the super-resolution and the side-lobe reduction. Please refer to [34] for more details of this part.

To summarize, the proposed method for 3-D SAR sparse imaging using Tensor Completion in embedded space is shown in Algorithm 1. It is clear that the incomplete data tensor is first transformed to an incomplete high order Hankel tensor by MDT. Next, the resulting higher order tensor is completed using low-rank tensor approximation and in the next step converted to the full-sampled data tensor by inverse MDT. Last, the 3-D image of the target can be reconstructed by applying the Fourier transform-based method.

Algorithm 1 3-D SAR Sparse Imaging using Tensor Completion in Embedded Space

Input: sparse data tensor $\mathcal{Y} \in \mathbb{C}^{M \times N \times K}$, a duplication matrix \mathbf{S}_1 , \mathbf{S}_2 and \mathbf{S}_3 , mask tensor

$\mathcal{Q} \in \{0,1\}^{M \times N \times K}$, the rank sequence $\{\mathbf{L}_1, \mathbf{L}_2, \dots, \mathbf{L}_I\}$, parameter τ , \mathcal{E} and tol.

Output: 3-D image \mathcal{I}

Initialization: $k_i \leftarrow 1$, $R_i \leftarrow \mathbf{L}_i(k_i)(\forall i)$, $\mathcal{G} \in \mathbb{C}^{R_1 \times R_2 \times \dots \times R_I}$, and $\{\mathbf{U}^{(i)}\}_{i=1}^I$

// Step 1: MDT

(1) duplicate tensor $\mathcal{Y} \leftarrow \mathcal{Y} \times_1 \mathbf{S}_1 \times_2 \mathbf{S}_2 \times_3 \mathbf{S}_3$

(2) folding operation $\mathcal{Y}_H \leftarrow \text{fold}_{(\Psi, \tau)}(\mathcal{Y})$

// Step 2: Tensor approximation

(3) $\mathcal{X} \leftarrow \mathcal{G} \times \{\mathbf{U}\}$

(4) $f_1 \leftarrow \|\mathcal{Q}_H \otimes (\mathcal{Y}_H - \mathcal{X})\|_F^2$

(5) **repeat**

(6) $\mathcal{Z} = \mathcal{Q}_H \otimes \mathcal{Y}_H + \bar{\mathcal{Q}}_H \otimes \mathcal{X}$

(7) **for** $i = 1$ to 6 **do**

(8) $\mathcal{Y}_H \leftarrow \mathcal{Z} \times_{-i} \{\mathbf{U}^T\}$

(9) $\mathbf{U}^{(i)} \leftarrow R_i$ leading singular vectors of $\mathbf{Y}_{(i)}$

(10) **end for**

(11) $\mathcal{G} \leftarrow \mathcal{Z} \times \{\mathbf{U}^T\}$

(12) $\mathcal{X} \leftarrow \mathcal{G} \times \{\mathbf{U}\}$

(13) $f_2 \leftarrow \|\mathcal{Q}_H \otimes (\mathcal{Y}_H - \mathcal{X})\|_F^2$

(14) **if** $|f_2 - f_1| \leq \text{tol}$ **then**

(15) $\tilde{\mathcal{X}} \leftarrow \mathcal{Q}_H \otimes (\mathcal{Y}_H - \mathcal{X})$

(16) $i' \leftarrow \arg \max_i \|\tilde{\mathcal{X}} \times_{-i} \{\mathbf{U}^T\}\|_F^2$

(17) $k_{i'} \leftarrow k_{i'} + 1$, and $R_{i'} \leftarrow \mathbf{L}_{i'}(k_{i'})$

(18) **else**

(19) $f_1 \leftarrow f_2$

(20) **end if**

(21) **until** $f_2 \leq \mathcal{E}$

(22) $\mathcal{X} \leftarrow \mathcal{G} \times \{\mathbf{U}\}$

// Step 3: IMDT

(23) Moore-Penrose pseudo-inverse $\mathbf{S}^\dagger \leftarrow (\mathbf{S}^T \mathbf{S})^{-1} \mathbf{S}^T$

(24) vectorization operation $\mathcal{H}_\tau^{-1}(\mathcal{X}) \leftarrow \text{unfold}_{(\Psi, \tau)}(\mathcal{X}) \times_1 \mathbf{S}_1^\dagger \times_2 \mathbf{S}_2^\dagger \times_3 \mathbf{S}_3^\dagger$

(25) obtain the completed tensor $\mathcal{X} \leftarrow \mathcal{H}_r^{-1}(\mathcal{X})$.

// Step 4: 3-D Image Reconstruction

(26) $\mathcal{I} = \text{3D-RD}(\mathcal{X})$, where 3D-RD represents 3-D Range Doppler (RD) algorithm. Please refer to [34] for more details of this part.

5 Results and Discussion

In this section, the effectiveness of the proposed 3-D imaging algorithm is evaluated by the simulated and real datasets. Our experiments are implemented in MATLAB R2019a environment using an Intel Core i9-9900KF, 3.60GHz processor with 128G of memory, and under Microsoft Windows 7 operating system.

5.1 Verification of the Proposed Algorithm using Simulated Dataset

First, the simulations of the 3-D distributed scene for DLSLA 3-D SAR are presented to confirm the validation of the proposed algorithm. An X-band SAR and a single scatterer located at (3m, 0m, -1m) are exploited in the simulations. The parameters of the simulations are listed in Table 1. A full-sample 3-D data in this simulation is collected by a uniform virtual linear array. The virtual linear array of 120 elements is built by using 4 transmit and 30 receive elements with MIMO technique. The Gaussian white noise is added to the raw data to have an SNR = 10dB. The first line in Fig.4 shows the 3-D imaging results by using 3-D FFT-based imaging method with full-sampled data.

Table 1 System Parameters of the Simulations

Parameter	Value
Center frequency (f_0)	10 GHz
Frequency step (Δf)	100 MHz
Signal Bandwidth (B_r)	150 MHz
Fly Height (H)	1000 m
Fly velocity (v)	200 m/s
Pulse Repeat Frequency (PRF)	1000 Hz
Number of range samples (K)	120
Number of azimuth samples (M)	200
Length of Linear array (L_y)	6 m

In the following simulations, the sparse sampling rate (SSR) is defined by the ratio of the number of observed samples to the number of all samples. Here, we use a sparse linear array by randomly selecting 60 elements to produce the sparse data. It can be calculated that the total sparse data is only 50% of the full data, i.e., SSR = 50%. This sparse data can be seen as a 3-D tensor data with the missing slice. For comparison, we pad the missing samples with zeros and then apply the different imaging algorithms to acquire 3-D images. The 3-D imaging results are illustrated in Fig.4. Images are obtained by the conventional 3-D RD method and the proposed method in the second and third line, respectively. For the proposed method, the missing slices are filled by using MDT and Tucker decomposition with the rank increment method. We set $\tau = (32, 1, 1)$ and a (120, 200, 120) echo data was converted into a (32, 89, 1, 200, 1, 120) tensor. The first and third modes can be ignored so this Hankel tensor was regarded as a fourth-order tensor with a size of (32, 89, 120, 200). Thus, the rank sequences for the proposed method were set as $\mathbf{L}_1 = [1 \ 2 \ 4 \ 8$

16 32], $\mathbf{L}_2 = [1\ 2\ 4\ 8\ 16\ 32\ 64\ 84]$, $\mathbf{L}_3 = [1\ 2\ 4\ 8\ 16\ 32\ 64\ 96\ 118]$, and $\mathbf{L}_4 = [1\ 2\ 4\ 8\ 16\ 32\ 64\ 96\ 128\ 160\ 192]$.

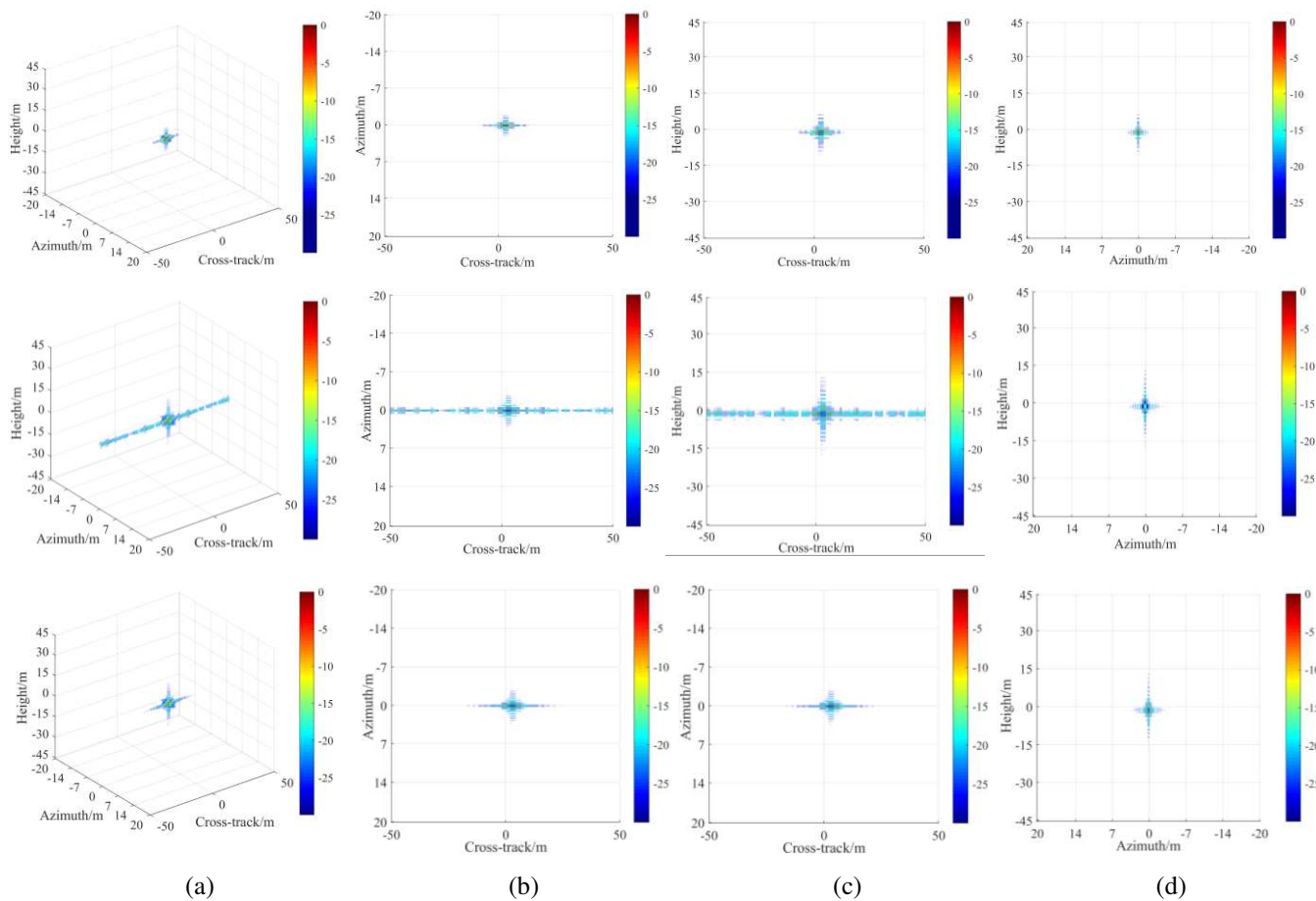


Fig.4 3-D imaging results by 3-D RD and proposed method with full-sampled data or sparse data. The SNR is chosen as 10dB. The amplitude of the 3-D image display is limited to be -25dB. From top to bottom, images are obtained by the conventional 3-D RD method with full-sampled data, the conventional 3-D RD method with sparse data and the proposed method with sparse data, respectively. From left to right, (a) 3-D imaging result, (b) Cross-track-azimuth slice, (c) Cross-tack-height slice, (d) Azimuth-height slice, respectively.

As we can see from Fig.4, the 3-D RD algorithm recovers the scatterer with high-level side-lobes along the cross-track direction for sparse data, whereas it can recover the image clearly with less side-lobes after TC processing with MDT in the proposed method. Noted that there is no significant change along both azimuth and height directions compared with the images based on full-sampled data because the missing slice is only appeared along the cross-tack direction. To quantitatively evaluate the imaging performance, a comparison of two indexes, i.e., the peak sidelobe ratio (PSLR) and integrated sidelobe ratio (ISLR) is utilized. These indexes can reflect some key features of SAR image, like the resolution and the sidelobe effect. Table 2 shows the evaluated indexes for the point target, where the best PSLR and ISLR values are emphasized in bold font. According to this quantitative evaluation, for the cross-track direction, PSLR and ISLR values of 3-D RD with sparse data deteriorate significantly, whereas the proposed method obtains the best performances. It is close to the corresponding indexes for 3-D RD with full-sampled data. Moreover, PSLR and ISLR values in the other two directions obtain the similar results among these algorithms.

Table 2 Evaluated Indexes for the Point Target

(X, Y, Z)	RD with full-sampled data	RD with 50% sparse data	Proposed method with 50% sparse data
PSLR(dB)	(-6.3010, -13.9317, -9.0579)	(-5.7059, -13.8840, -8.5366)	(-6.3652, -13.9663, -9.1599)
ISLR(dB)	(-6.2692, -4.1744, -2.7365)	(-1.9645, -3.9009, -2.5161)	(-6.3401, -4.2311, -2.7787)

5.2 Performance Comparison with Different algorithms

Furthermore, the performance of the proposed method is compared with those of other different algorithms including the conventional tensor completion algorithms: high accuracy low rank tensor completion (HaLRTC) and Tucker decomposition (TDC) and compressive sensing algorithm. A target composed of ten point scatterers with equal amplitude is chosen in this simulations. Fig.5 shows the 3-D imaging result by using 3-D FFT-based imaging method with full-sampled data, which can be seen as a standard image for comparison among different imaging algorithms with sparse-sampled data.

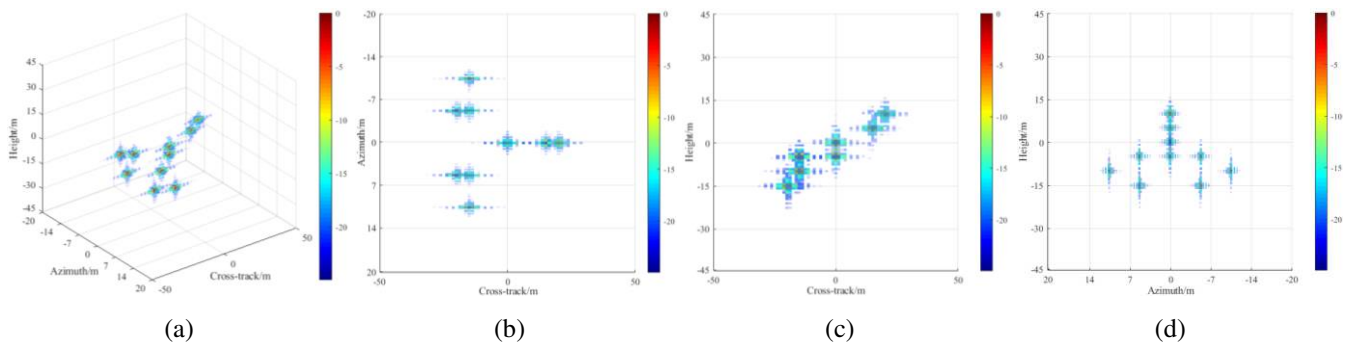


Fig.5 3-D imaging result by 3-D RD with full-sampled data. The SNR is chosen as 10dB. The amplitude of the 3-D image display is limited to be -25dB. (a) 3-D imaging result. (b) Cross-track-azimuth slice. (c) Cross-tack-height slice. (d) Azimuth-height slice.

Fig.6 illustrates the 3-D imaging results obtained by different algorithms. From top to bottom, images are obtained by the 3-D RD method, the HaLRTC-based method, the TDC-based method and the proposed method, respectively. The 3-D tensor data with 80% random missing slices along the cross-track direction, i.e., SSR = 80%. From left to right, the 3-D imaging result and its 3-D views on cross-track-azimuth slice, cross-track-height slice and azimuth-height slice, respectively. Comparing Fig.6 with referenced Fig.5, it can be seen evidently that although the scatterers can be resolvable using the conventional 3-D RD method with sparse data, the influence of high side-lobes is obviously increased along the cross-track direction because of the lack of enough data samples. As shown in the second and third lines, HaLRTC and TDC fail to recover the missing slices, which lead to the invalid suppression of side-lobes in 3-D imaging result. By contrast, the imaging results obtained by the proposed method can recover the scatterers clearly with the suppression of side-lobes, which can produce nearly the similar 3-D imaging performance with the full data in Fig.5. Similar to the results from Fig.4, the imaging performance along the azimuth and height direction changes between different methods with sparse data are not obvious.

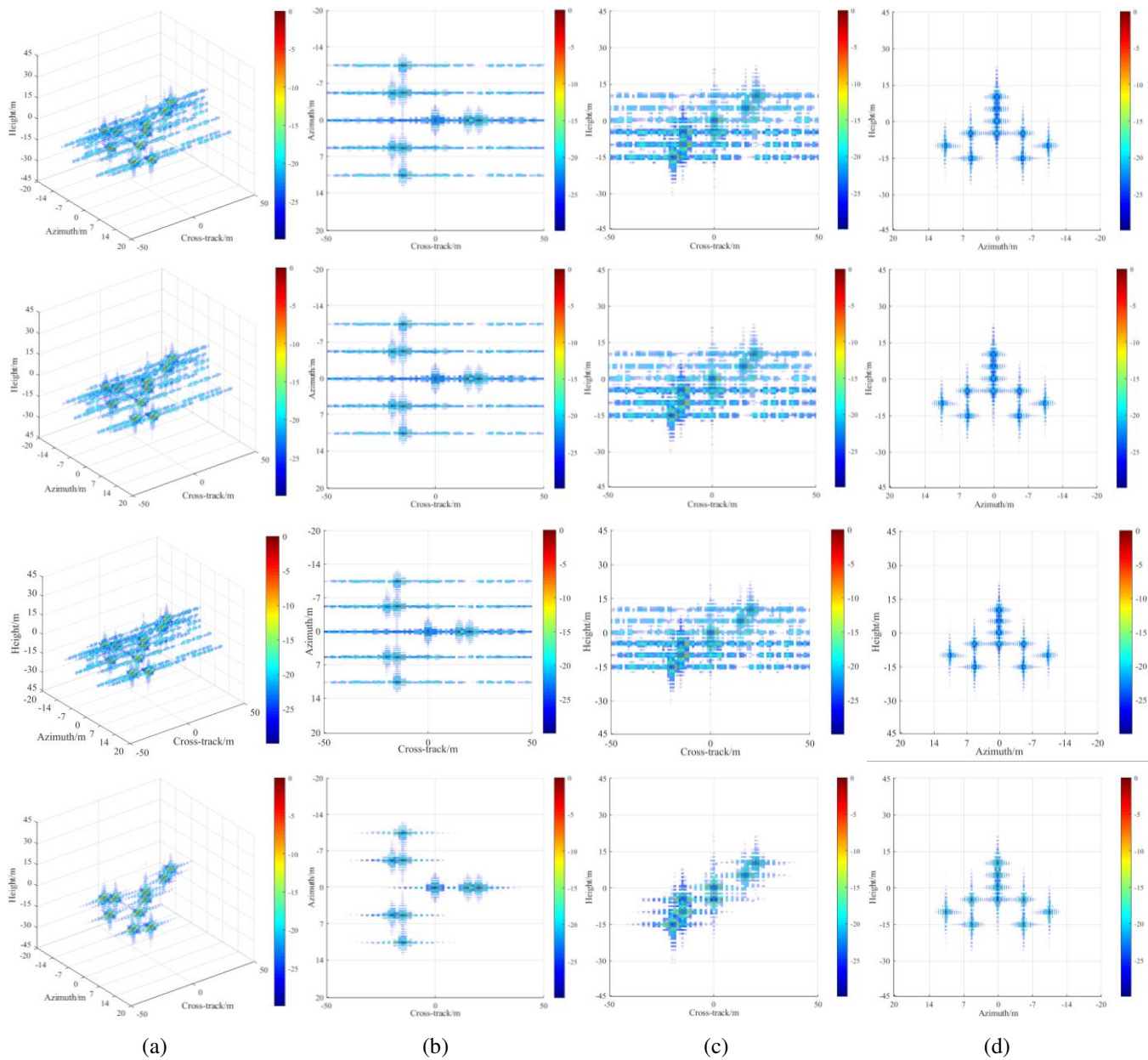


Fig.6 Comparison of 3-D imaging results by different methods with sparse data. From top to bottom, images are obtained by the conventional 3-D RD method, the HaLRTC-based method, the TDC-based method and the proposed method, respectively. From left to right, the 3-D imaging result and its 3-D views on cross-track-azimuth slice, cross-track-height slice and azimuth-height slice, respectively. The SNR is chosen as 10dB. The amplitude of the 3-D image display is limited to -25dB.

5.3 Performance with Different SSRs and SNRs

Although the proposed method is able to recover the missing slices to obtain the 3-D image perfectly with suppression of sidelobes, the SSR and SNR still play an important role in the imaging performance. To quantitatively evaluate the imaging performance, the estimated error of the 3-D imaging result is utilized, which can be defined as

$$MSE = \frac{\|\mathcal{X}_r - \mathcal{X}_0\|_F}{\|\mathcal{X}_0\|_F} \quad (29)$$

where \mathcal{X}_r and \mathcal{X}_0 are 3-D images reconstructed with sparse data and full data, respectively. A smaller MSE usually indicates a better reconstruction performance.

To illustrate the imaging performance with different SSRs, we test different SSRs from 10% to 90% under Monte Carlo simulation. The SNR is chosen to be 10dB. The average MSE is calculated over 50 Monte-Carlo trials. Fig.7 shows the comparison result of average MSEs between four different methods based on sparse data with varying sparse sampling rates. It can be seen clearly that the average MSEs of the 3-D RD method, the HaLRTC-based method and the TDC-based method are overlap totally because the HaLRTC-based and the TDC-based methods are invalid completely. With the increase of SSR, the average MSE of all methods is reduced and reconstruction accuracy is improved as well. Among these curves, when the SSR is more than nearly 30%, the recovery error of the proposed method is extremely low (almost less than 0.1), whereas the average MSE increases drastically when the SSR is less than 30%. It demonstrates that, if SSR is not excessively low (e.g. 30%), the 3-D imaging result of the proposed method is reliable.

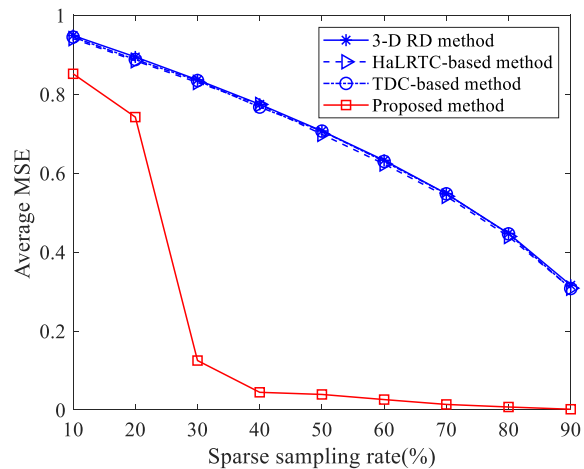


Fig.7 Average MSE between different methods based on sparse data with varying sparse sampling rates. The SNR is chosen to be 10dB.

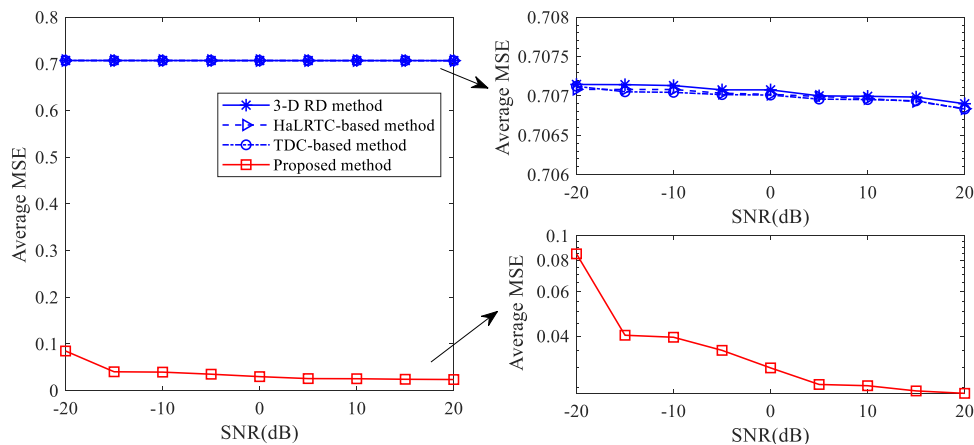


Fig.8 Average MSE between different methods based on sparse data with varying SNRs. The sparse sampling rate is set as 50%.

In order to evaluate the performance of the proposed method in the presence of noise, SNRs ranging from -20dB to 20dB are examined under Monte Carlo simulation. The number of Monte Carlo trials is 50. The average MSE is calculated for each SNR level and plotted in Fig.8. Noted that the variables \mathcal{X}_r and \mathcal{X}_0 in eq. (29) are denoted as 3-D images reconstructed with sparse data and full data at the same SNR level, respectively. Although we found that the fluctuation of the curves with 3-D RD method, HaLRTC-based method and TDC-based method are not prominent, the average MSEs are slightly reduced with the increasing of SNR according to the detail view in the upper right corner of Fig.8. Moreover, with the increased SNR, the MSE goes down

remarkably and when the SNR reaches -20dB , the value of average MSE for the proposed method is still less than 0.1, which implies that satisfactory 3-D imaging results can be obtained by the proposed method with a relatively low SNR. Even so, we can observe from the detail view in the lower right corner that there appears a transition point at the curve of -15dB , which indicates when the SNR is very low (less than -15dB), the increment of error becomes larger.

5.4 Verification of the Proposed Algorithm using Real Dataset

To illustrate the validity and the advantages of the proposed algorithm, the experimental results based on raw radar data are presented. The data acquisition geometry of the system is shown in Fig.9. We control the motions of the transmitter and the receiver antennas to synthesize a virtual 2-D antenna array. A principle prototype experimental system for DLLA 3-D SAR with a random sparse linear array consists of the radar module and the motion-control module, as shown in Fig.10(a) and (b). The radar module, working at X-band, mainly transmits and receives step frequency signals. High range resolution is obtained by utilizing the full band step frequency measurements. The motion-control module mainly controls the motions of one transmit-receive pair located on a 2-D planar aperture rail. The 2-D horizontal apertures are formed by manually changing the antenna positions and repeating the data acquisition process. Eight foamy cubes covered with tinfoil [see Fig.10(c)] are laid on the foamy platform hung near the ceiling [see Fig.10(d)] with different heights. The experimental parameters are listed in Table 3.

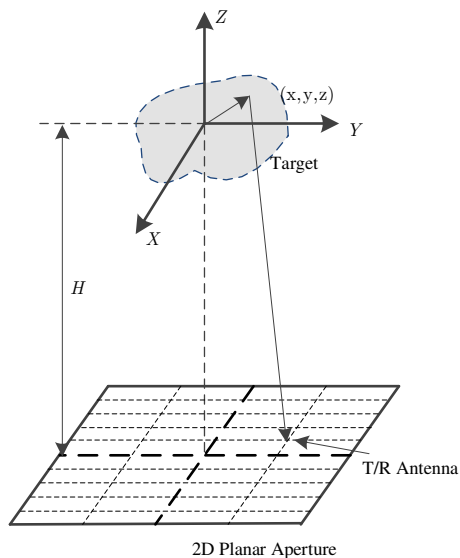


Table 3 Experiment Parameters on Real Data

Parameter	Value
Transmitted Frequency	8-12GHz
Full Sweep Bandwidth	4GHz
Frequency Step	1MHz
Center Height	2.2m
Azimuth Sampling Number	161
Cross-track Sampling Number	50
Azimuth Sampling Space	0.01m
Cross-track Sampling Space	0.02m

Fig.9 Data acquisition geometry of the principle prototype experiment.

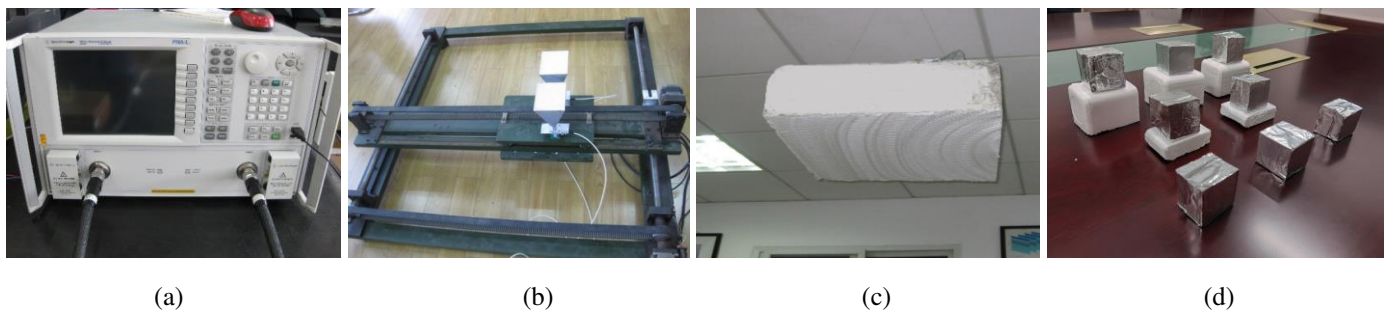


Fig.10 DLLA 3-D SAR system with sparse linear array. (a) Two-dimensional planar rail. (b) Vector network analyzer. (c) Foamy platform. (d) Eight targets covered with tinfoil.

In the experiment, the size of the tensor is $(50, 161, 1601)$. The proposed method is applied with $\tau = (32, 1, 1)$ for the given

tensor. The rank sequences are set as $\mathbf{L}_1 = [1\ 2\ 4\ 8\ 16\ 32]$, $\mathbf{L}_2 = [1\ 2\ 4\ 8\ 16]$, $\mathbf{L}_3 = [1\ 2\ 4\ 8\ 16\ 32\ 64\ 96\ 128\ 160]$, and $\mathbf{L}_4 = [1\ 2\ 4\ 8\ 16\ 32\ 64\ 128\ 256\ 512\ 1024]$. Fig.11 demonstrates the 3-D images reconstructed by various methods based on sparse data with missing slices. Similar to the above simulations, the ordinary low-rank model could not recover the missing slices for real data, whereas the results obtained by the proposed method are very clear, although their accuracy are not high. At the same time, the comparison results by four methods with different SSRs are also shown in Fig.11. With the decrease number of samples, all of the methods obtain more blurred images. When the SSR reaches 20%, the targets can not distinguish at all by 3-D RD and HaLRTC-based method and TDC-based method produced similar results. By contrast, the proposed method obtains significant improvements compared with the other methods. Table 4 shows the average MSE results obtained for all of the completion methods with three different SSRs, which demonstrates that the proposed method performs better than the other methods and it was also very robust in terms of the SSR.

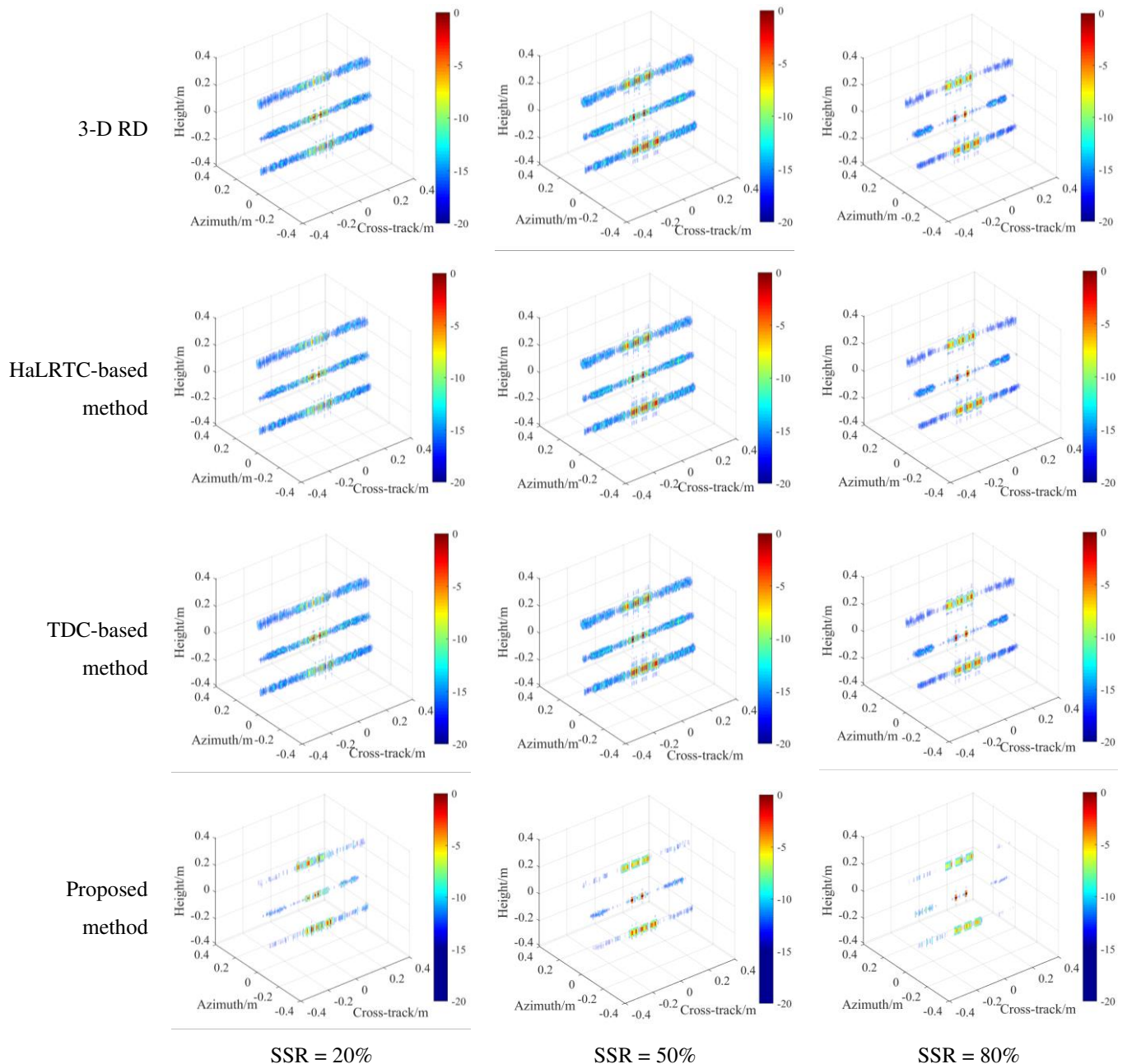


Fig.11 Comparison of 3-D imaging results by sparse data completed with various methods.

Table 4 Average MSE results obtained for all of the completion methods with three different SSRs

Method	Average MSE		
	SSR = 20%	SSR = 50%	SSR = 80%
3-D RD	0.9215	0.7096	0.4458
HaLRTC-based method	0.9215	0.7096	0.4458
TDC-based method	0.9215	0.7096	0.4458
Proposed method	0.4648	0.2558	0.1191

6 Conclusion

In this paper, we proposed a novel 3-D SAR imaging algorithm for DLLA 3-D SAR with sparse linear array using tensor completion in embedded space. With the help of sparsity and low-rank property, the 3-D signal reconstruction has been developed based on transforming the incomplete data to a multiway delay embedded space and using Tucker decomposition to perform reconstruction. First, Hankelization approach has been introduced by transforming the incomplete echo data to a higher order tensor. Then low-rank Tucker decomposition has been applied for completion, where the ranks of the core tensors were increasing gradually using a proposed rank incremental strategy. After the above TC processing, the conventional algorithm can easily get the satisfactory 3-D images. The main feature of the proposed algorithm is that of allowing high resolution and low side-lobes with respect to other match filter-based methods, considering the elements in some continuous slices are missing in the data tensor caused by the sparse linear array.

Numerical results on simulated data and real data show clearly that the proposed algorithm can effectively suppress the adverse effects, including high-level side-lobes, even the appearance of the aliasing and false-alarm targets caused by the sparse data with missing slices. Compared with the 3-D RD and state-of-the-art tensor completion algorithms, the imaging result obtained by the proposed algorithm can recover the targets clearly with the suppression of side-lobes, which is similar to the imaging performance with the full data. The imaging performance is also verified across different SSR and SNR values, which implies that the proposed algorithm performs better and it was also robust in terms of the SSRs and SNRs.

Note that the theoretical derivation of signal model in this paper is based on the first-order Taylor expansion approximation. It is only suitable for the research of point targets in three-dimensional scenes. In the future, 3D imaging will be further deeply studied for area targets with the distributed characteristics.

Abbreviations

TC: Tensor completion; MDT: Multiway delay embedding transform; 3D: Three-dimensional; SAR: Synthetic Aperture Radar; InSAR: Interferometric SAR; CSAR: Circular SAR; LASAR: Linear array SAR; DLLA: Downward-looking linear array; CS: Compressive sensing; ALS: Alternating least squares; RD: Range Doppler; DLSLA: Downward looking sparse linear array; MIMO: Multiple input multiple output; SSR: Sparse sampling rate; SNR: Signal noise ratio; PSLR: Peak sidelobe ratio; ISLR: Integrated sidelobe ratio; HaLRTC: High accuracy low rank tensor completion; TDC: Tucker decomposition; FFT: Fast Fourier transform; MSE: Mean square error.

Acknowledgements

The authors would like to thank the handing Associate Editor and the anonymous reviewers for their valuable comments and suggestions for this paper.

Funding

This work was supported by the National Natural Science Foundation of China under Grant 61701508 and Hunan Provincial

Natural Science Foundation of China under Grant 2018JJ3613.

Authors' contributions

Siqian Zhang designed the work, developed the approach, analyzed and interpreted the data, and drafted the manuscript; Ding Ding and Lingjun Zhao contributed to literature investigation; Chenxi Zhao contributed to revise the manuscript. Both authors read and approved the final manuscript.

Availability of data and materials

Please contact author for data requests.

Competing interests

The authors declare that they have no competing interests.

Author details

¹ State Key Laboratory of Complex Electromagnetic Environment Effects on Electronics and Information System, College of Electronic Science, National University of Defense Technology, Changsha 410073, China.

² Center for Teaching and Research Service, National University of Defense Technology, Changsha 410073, China.

References

- [1] Budillon, A., Evangelista, A., Schirinzi, G.: Three-dimensional SAR focusing from multipass signals using compressive sampling. *IEEE Trans. Geosci. Remote Sens.* 49(1), 488-499 (2011).
- [2] Massonnet, D., Rabaute, T.: Radar interferometry: Limits and potential. *IEEE Trans. Geosci. Remote Sens.* 31(2), 455-464 (1993).
- [3] Zhu, X., Bamler, R.: Demonstration of Super-Resolution for Tomographic SAR Imaging in Urban Environment. *IEEE Trans. Geosci. Remote Sens.* 50(8), 3150-3157 (2012).
- [4] Ponce, O., Prats-Iraola, P., Pinheiro, M., Rodriguez-Cassola, M., Moreira, A.: Fully-Polarimetric High-Resolution 3-D Imaging with Circular SAR at L-Band. *IEEE Trans. Geosci. Remote Sens.* 52(6), 1-17 (2013).
- [5] Ponce, O., Prats, P., Rodriguez-Cassola, M., Scheiber, R., Reigber, A.: Processing Of Circular SAR Trajectories With Fast Factorized Back-Projection. Paper presented at the 2011 IEEE International Geoscience and Remote sensing Symposium, Vancouver, BC, Canada, 24-29 July 2011 (2011).
- [6] Wen, H.: Progress in Circular SAR Imaging Technique. *Journal of Radars.* 1(2), 124-135 (2012).
- [7] Bao, Q., Peng, Q., Wang, Z., Lin, Y., Hong, W.: DLSLA 3-D SAR Imaging Based on Reweighted Gridless Sparse Recovery Method. *IEEE Geosci. Remote Sens. Lett.* 13(6), 841-845 (2017).
- [8] Zhang, S., Dong, G., Kuang, G.: Matrix Completion for Downward-Looking 3-D SAR Imaging With a Random Sparse Linear Array. *IEEE Trans. Geosci. Remote Sens.* 56(4), 1994-2006 (2017).
- [9] Gu, T., Liao, G., Li, Y., Liu, Y., Guo, Y.: Airborne Downward-Looking Sparse Linear Array 3-D SAR Imaging via 2-D Adaptive Iterative Reweighted Atomic Norm Minimization. *IEEE Trans. Geosci. Remote Sens.* 60(99), 1-13 (2021).
- [10] Liao, Y., Xing, M., Zhang, L., Bao, Z.: A novel modified Omega-K algorithm for circular trajectory scanning SAR imaging using series reversion. *EURASIP Journal on Advances in Signal Processing.* 2013(1), 1-12 (2013).
- [11] Gierull, C.: On a concept for an airborne downward-looking imaging radar. *AEU - International Journal of Electronics and Communications.* 53(6), 295-304 (1999).
- [12] Zhang, S., Yu, M., Kuang, G.: Tensor RPCA for Downward-Looking 3-D SAR Imaging with Sparse Linear Array. Paper presented at 15th IEEE International Conference on Signal Processing (ICSP), Beijing, China, 6-9 Dec. 2020 (2020).

- [13] Wei, M., Ender, J.,: A 3D imaging radar for small unmanned airplanes - ARTINO. Paper present at European Radar Conference, Paris, France, 3-4 Oct. 2005 (2005).
- [14] Nouvel, J., Jeuland, H., Bonin, G., Roques, S., Du, O., Peyret, J.,: A Ka Band Imaging Radar: DRIVE on Board ONERA Motorglider. Paper presented at 2006 IEEE International Conference on Geoscience Remote Sensing Symposium, Denver, CO, USA, 31 July - 4 Aug. 2006 (2006).
- [15] Ren, X., Yang, J., Chen, L.,: 3D Imaging Algorithm for Down-Looking MIMO Array SAR Based on Bayesian Compressive Sensing. *International journal of antennas and propagation*. 2014, 9 (2014).
- [16] Zhang, S., Dong, G., Kuang, G.,: Superresolution Downward-Looking Linear Array Three-Dimensional SAR Imaging Based on Two-Dimensional Compressive Sensing. *IEEE Journal of Selected Topics in Applied Earth Observations Remote Sensing*. 9(6), 2184-2196 (2016).
- [17] Wei, Q., Martorella, M., Zhou, J., Zhao, H., Qiang, F.,: Three-dimensional inverse synthetic aperture radar imaging based on compressive sensing. *IET Radar, Sonar Navigation*. 9(4), 411-420 (2015).
- [18] Liu, J., Musialski, P., Wonka, P., Ye, J.,: Tensor Completion for Estimating Missing Values in Visual Data. *IEEE Transactions on Pattern Analysis and Machine Intelligence*. 35(1), 208-220 (2013).
- [19] Zheng, Y., Huang, T., Ji, T., Zhao, X., Jiang, T., Ma, T.,: Low-rank tensor completion via smooth matrix factorization. *Applied Mathematical Modelling*. 70, 677-695 (2019).
- [20] Kolda, T.,: Tensor decompositions and applications. *Siam Review*. 51(3), 455-500 (2009).
- [21] Yan, J., Pu, W., Zhou, S., Liu, H., Bao, Z., Collaborative detection and power allocation framework for target tracking in multiple radar system. *Information Fusion*. 55, 173-183 (2020).
- [22] Yan, J., Dai, J., Pu, W., Liu, H., S. Greco, M.,: Target Capacity based Resource Optimization for Multiple Target Tracking in Radar Network. *IEEE Transactions on Signal Processing*. 69(99), 2410-2421 (2021).
- [23] He, W., Yokoya, N., Yuan, L., Zhao, Q.,: Remote Sensing Image Reconstruction Using Tensor Ring Completion and Total Variation. *IEEE Trans. Geosci. Remote Sens.* 57(99), 8998-9009 (2019).
- [24] Zhang, J., Qin, M., Bai, C., Zheng, J.,: Missing Elements Recovery Using Low-Rank Tensor Completion and Total Variation Minimization. Springer, Singapore, 2019.
- [25] Qiu, W., Zhou, J., Fu, Q.,: Tensor Representation for Three-Dimensional Radar Target Imaging With Sparsely Sampled Data. *IEEE Transactions on Computational Imaging*. 6, 263-275 (2019).
- [26] Feng, W., Friedt, J., Nico, G.,: 3-D Ground-Based Imaging Radar Based on C-Band Cross-MIMO Array and Tensor Compressive Sensing. *IEEE Geoscience and Remote Sensing Letters*. 16(10), 1585-1589 (2019).
- [27] Sedighin, F., Cichocki, A., Yokota, T., Shi, Q.,: Matrix and Tensor Completion in Multiway Delay Embedded Space Using Tensor Train, With Application to Signal Reconstruction. *IEEE Signal Processing Letters*. 27(99), 810-814 (2020).
- [28] Yokota, T.,: Missing Slice Recovery for Tensors Using a Low-rank Model in Embedded Space. Paper presented at 2018 Proceedings of IEEE Conference on Computer Vision and Pattern Recognition. *IEEE Computer Society Conference on Computer Vision and Pattern Recognition*, Lake City, UT, USA, 18-23 June 2018 (2018).
- [29] Dai, J., Q. Jin, Y.,: Scattering Simulation and Reconstruction of a 3-D Complex Target Using Downward-Looking Step-Frequency Radar. *IEEE Trans. Geosci. Remote Sens.* 49(10), 4035-4047 (2011).
- [30] Li Y., Liu, K., Razavilar, J.,: A parameter estimation scheme for damped sinusoidal signals based on low-rank Hankel approximation. *IEEE Transactions on Signal Processing*. 45(2), 481-486 (1997).
- [31] Filipovi, M., Juki, A.,: Tucker factorization with missing data with application to low-rank tensor completion. Kluwer Academic Publishers. 26(3), 677-692 (2015).

- [32] Wang, J., Zhao, G., Wang, D., Li, G.: Tensor Completion using Low-Rank Tensor Train Decomposition by Riemannian optimization. Paper presented at 2019 Chinese Automation Congress (CAC), Hangzhou, China, 22-24 Nov. 2019(2019).
- [33] Zhang, S., Zhu, Y., Kuang, G.: Imaging of downward-looking linear array three-dimensional SAR Based on FFT-MUSIC. *IEEE Geoscience and Remote Sensing Letters*. 12(4), 885-889 (2015).
- [34] Du, L., Wang, Y., Hong, W., Tan, W., Wu, Y.: A Three-Dimensional Range Migration Algorithm for Downward-Looking 3D-SAR with Single-Transmitting and Multiple-Receiving Linear Array Antennas. *Eurasip Journal on Advances in Signal Processing*. 2010(1), 11 (2010).